

Metallicity and star formation activities of the interacting system Arp 86 from observations with MOS on the Xinglong 2.16 m telescope *

Zhi-Min Zhou, Hong Wu, Lei Huang, Hong-Bin Li, Zhi-Zhong Zhou, Jun-Jun Jia,
Man-I Lam and Yi-Nan Zhu

Key Laboratory of Optical Astronomy, National Astronomical Observatories, Chinese Academy of Sciences, Beijing 100012, China; zmzhou@bao.ac.cn

Received 2014 January 10; accepted 2014 April 26

Abstract We present an analysis of the metallicity and star formation activities of H II regions in the interacting system Arp 86, based on the first scientific observations using multi-object spectroscopy with the 2.16 m telescope at the Xinglong Observing Station. We find that the oxygen abundance gradient in Arp 86 is flatter than that in normal disk galaxies, which confirms that gas inflows caused by tidal forces during encounters can flatten the metallicity distributions in galaxies. The companion galaxy NGC 7752 is currently experiencing a galaxy-wide starburst with a higher star formation rate surface density than the main galaxy NGC 7753, which can be explained in that the companion galaxy is more susceptible to the effects of interaction than the primary. We also find that the galaxy 2MASX J23470758+2926531 has similar abundance and star formation properties to NGC 7753, and may be a part of the Arp 86 system.

Key words: galaxies: abundances — galaxies: evolution — galaxies: interactions — (ISM:) H II regions — techniques: spectroscopic

1 INTRODUCTION

Gravitational interactions and mergers play a major role in galaxy evolution, drastically modifying both their morphology and star formation activities (Barnes & Hernquist 1992; Hopkins et al. 2010). Detailed investigations of individual interacting galaxies can provide important information about the physics of the encounter, including the enhancement or suppression of star formation (SF), as well as hydrodynamical processes (Struck & Smith 2003).

The metallicity distribution and the properties of stellar populations in galaxies are important for understanding the physical processes in the formation and evolution of galaxies and have been studied by many authors (e.g., Wu et al. 2005b; Zhou et al. 2011). Extragalactic H II regions represent perfect laboratories for deriving the physical properties of gaseous nebulae and star clusters across the surface of nearby galaxies (Osterbrock & Ferland 2006). Their characteristic emission-line spectra have been extensively used to probe stellar populations and chemical composition of

* Supported by the National Natural Science Foundation of China.

local star-forming galaxies, which can provide observational tests for mechanisms related to galaxy evolution (Bresolin et al. 2012; Li et al. 2013).

Multi-object spectroscopy (MOS) offers the possibility of obtaining spectra of tens to hundreds of objects simultaneously. The development of MOS instruments at ground-based telescopes provides an opportunity to derive the physical properties of interacting galaxies using optical spectra of their associated ionized gas.

In the current study, we present spectroscopic observations of an interacting system Arp 86 with the help of MOS, to probe the metallicity, star formation rates (SFRs) and stellar populations of its H II regions, in an attempt to study the impact of interaction on the evolution of galaxies. Arp 86 is an interacting galaxy pair resembling the M51 system with a redshift of $z \sim 0.0162$ from the NASA/IPAC Extragalactic Database (NED). The galaxy pair consists of a grand design spiral galaxy NGC 7753 and a small companion NGC 7752. NGC 7753 is an SAB galaxy with a radius $R_{25} \sim 1'$ (corresponding to 20 kpc), which is defined by the isophote at the brightness of 25 mag arcsec⁻² in the *B*-band. A tidal bridge connecting the two galaxies is found in the optical images and active star formation is occurring in the two galaxies and the bridge (Laurikainen et al. 1993). The infrared luminosity (8–1000 μ m) of Arp 86 is $10^{11.01} L_{\odot}$ (Sanders et al. 2003), indicating that it is a luminous infrared galaxy (LIRG) system. Radio continuum observations show a complex distribution of H I tails and bridges due to tidal interactions (Sengupta et al. 2009). H I maps show that the compact dwarf galaxy 2MASX J23470758+2926531 lying toward the southeast of Arp 86 may also be a part of this system (Sengupta et al. 2009).

The layout of this article is as follows: in Section 2, we introduce the selection of target star-forming regions for spectra, together with a description of the observations and data reduction procedures. In Section 3, we present and analyze the observational results, including dust extinction, excitation properties, metallicities and star formation activities. The results are discussed and interpreted in Section 4 and then summarized in Section 5.

2 OBSERVATIONS AND DATA

In this section, we first briefly describe the selection of the target H II regions in Arp 86. The instrument we used and observations are presented next. Then the data reduction and line flux measurement are introduced.

2.1 Sample Selection

We selected the target H II regions from a narrowband H α image of Arp 86, which was obtained by the BAO Faint Object Spectrograph and Camera (BFOSC) attached to the 2.16 m telescope at the Xinglong Observing Station administered by National Astronomical Observatories of the Chinese Academy of Sciences. The bright H II regions were manually selected in the bulge and disks. In order to avoid selection biases, some faint candidates were also included along with the bright ones.

Finally, 69 sources were selected; their spatial locations are shown in Figure 1. The astronomical coordinates and identification data of these regions are presented in Table 1. Besides the targets in Arp 86, the object 2MASX J23470758+2926531 was also selected (No.70 in Fig. 1).

2.2 Instrument and Observation

We obtained optical spectroscopy of H II region candidates with the MOS at the f/9 Cassegrain focus of the Xinglong 2.16 m telescope. The MOS is attached in the spectroscopic mode of BFOSC, the same instrument used to take the narrowband H α image. The E2V CCD detector that is used with MOS has 22.5 μ m square pixels, yielding an image scale of 0.457'' pixel⁻¹ and a field of view (FoV) of $\sim 8.5' \times 9.5'$. The MOS instrument can observe ten to one hundred targets simultaneously.

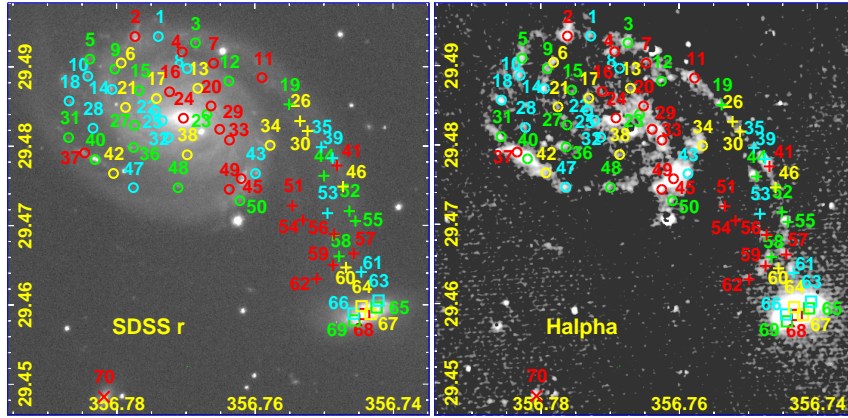


Fig. 1 Images of Arp 86, identifying the target H II regions. The background images are SDSS r (left) and $H\alpha$ (right) images of Arp 86 with the target H II regions labeled. The symbols indicate the different data locations: circles – the dominant galaxy NGC 7753, squares – the companion galaxy NGC 7752, pluses – the tidal bridge between the two galaxies, and cross – the galaxy 2MASX J23470758+2926531. There are four colors and the targets with the same color were observed in the same mask. Region numbers are labeled in the figure and correspond to those given in Table 1.

Table 1 Sample of Observed H II Regions

ID	R.A. (J2000.0)	Dec. (J2000.0)	[O II] $\lambda 3727$	[O III] $\lambda 5007$	$H\alpha$	[N II] $\lambda 6583$	[S II] $\lambda\lambda 6717, 6731$	$c(H\beta)$	$12+\log(O/H)$	$\log SFR$ ($M_{\odot} \text{ yr}^{-1}$)
1	23:47:05.68	29:29:37.68	187(13)	25.4(7.4)	125(3)	44.0(2.9)	47.2(7.8)	1.05	8.64	-1.34
2	23:47:06.49	29:29:37.67	47.7(2.9)	18.2(1.9)	82.1(0.8)	28.5(0.7)	28.0(1.4)	0.04	8.64	-1.52
3	23:47:04.39	29:29:34.78	15.4(4.8)	48.3(5.8)	126(3)	45.6(3.2)	68.3(6.1)	0.91	8.65	-1.33
4	23:47:04.85	29:29:30.68	24.8(5.5)	...	32.9(1.6)	15.2(1.5)	22.8(2.2)	0.49	8.71	-1.92
5	23:47:08.06	29:29:27.40	53.1(3.3)	...	128(2)	46.7(2.0)	42.6(3.3)	0.63	8.65	-1.32
6	23:47:06.97	29:29:25.68	124(14)	...	257(5)	110.8(5.0)	76.4(10.7)	1.24	8.69	-1.02
7	23:47:03.76	29:29:25.52	11.0(0.9)	5.41(0.82)	13.7(1.3)	0.22	8.72	-2.39
8	23:47:04.68	29:29:23.19	12.5(1.8)	8.41(2.16)	6.57(2.89)	0.51	8.80	-2.34
9	23:47:07.19	29:29:22.90	12.4(0.9)	6.45(4.67)	26.8(0.9)	12.4(0.9)	14.6(2.3)	0.14	8.71	-2.00
10	23:47:08.13	29:29:19.69	59.6(1.9)	17.6(0.9)	50.0(1.6)	0.61	8.60	-1.66
11	23:47:02.08	29:29:18.99	22.2(3.6)	1.90(1.93)	20.9(1.1)	9.99(1.34)	23.4(2.1)	0.29	8.72	-2.11
12	23:47:03.23	29:29:17.46	34.8(2.9)	2.14(2.05)	43.7(1.9)	18.1(1.3)	20.7(3.1)	0.53	8.68	-1.79
13	23:47:04.31	29:29:14.17	44.0(3.0)	24.2(3.9)	34.1(6.9)	...	8.75	-1.79
14	23:47:07.29	29:29:13.69	91.5(1.5)	32.2(1.0)	24.7(2.1)	0.39	8.64	-1.47
15	23:47:06.34	29:29:13.18	3540(266)	119(53)	285(32)	140(25)	159(31)	2.23	8.73	-0.98
16	23:47:05.29	29:29:12.59	31.3(53.6)	7.13(4.29)	25.8(2.8)	14.4(4.3)	33.9(4.5)	1.02	8.76	-1.69
17	23:47:05.75	29:29:09.54	55.2(2.7)	13.2(3.9)	29.1(3.9)	...	8.55	-1.76
18	23:47:08.78	29:29:08.43	9.07(0.59)	...	62.3(0.8)	21.0(0.7)	16.8(1.3)	0.03	8.63	-1.64
19	23:47:01.14	29:29:06.87	36.3(3.9)	24.8(3.2)	53.3(1.8)	20.4(2.0)	35.3(5.3)	0.71	8.66	-1.71
20	23:47:03.85	29:29:06.14	169(33)	...	50.5(3.1)	26.1(6.5)	42.6(5.7)	1.08	8.74	-1.73
21	23:47:06.82	29:29:05.50	23.3(1.2)	8.39(1.12)	9.66(2.04)	...	8.65	-2.06
22	23:47:05.79	29:29:03.81	34.2(1.8)	12.6(2.2)	14.9(5.4)	...	8.65	-1.90
23	23:47:03.99	29:29:02.33	49.4(4.6)	10.3(4.2)	43.9(3.1)	12.6(3.4)	18.6(2.6)	0.90	8.59	-1.79
24	23:47:04.81	29:29:00.60	12569(1535)	...	2650(49)	2790(43)	897(40)	2.28	8.91	-0.01
25	23:47:05.55	29:28:59.50	18.5(2.3)	10.1(2.9)	9.91(2.49)	0.69	8.75	-2.17
26	23:47:00.76	29:28:59.29	42.7(5.1)	19.4(2.7)	30.2(2.1)	11.4(2.4)	20.6(2.6)	0.78	8.66	-1.95

Table 1 — *Continued*

ID	R.A. (J2000.0)	Dec. (J2000.0)	[O II] λ3727	[O III] λ5007	Hα	[N II] λ6583	[S II] λλ6717,6731	c(Hβ) 12+log(O/H)	log SFR (M _⊙ yr ⁻¹)	
27	23:47:06.51	29:28:57.31	18.8(1.4)	6.07(1.19)	10.4(2.3)	...	8.62	-2.16
28	23:47:07.95	29:28:56.06	409(37)	103(31)	276(8)	95.5(7.8)	66.0(21.3)	1.60	8.64	-0.99
29	23:47:03.55	29:28:55.58	42.3(12.0)	3.60(3.54)	60.9(2.7)	16.0(3.1)	40.0(4.0)	0.87	8.57	-1.65
30	23:47:00.50	29:28:54.78	83.0(11.9)	22.3(9.7)	72.0(3.8)	30.7(3.4)	45.9(6.6)	1.12	8.69	-1.58
31	23:47:08.80	29:28:51.85	66.6(3.1)	...	53.2(1.3)	16.0(1.1)	22.6(3.1)	0.44	8.60	-1.71
32	23:47:05.34	29:28:51.81	...	137(104)	240(31)	102(29)	55.3(29.1)	2.23	8.69	-1.05
33	23:47:03.21	29:28:50.68	32.7(18.9)	14.7(5.9)	84.0(2.4)	30.0(3.1)	48.9(4.8)	0.91	8.64	-1.51
34	23:47:01.80	29:28:48.28	457(35)	48.2(11.1)	183(7)	65.5(7.0)	103(10)	1.47	8.65	-1.17
35	23:47:00.02	29:28:47.44	17.1(2.4)	4.78(3.04)	9.21(3.56)	...	8.58	-2.20
36	23:47:06.54	29:28:47.34	39.2(1.5)	16.6(1.6)	19.0(2.8)	0.46	8.69	-1.84
37	23:47:08.24	29:28:45.00	469(62)	107(35.7)	214(6)	77.4(5.5)	118(16.4)	1.27	8.65	-1.10
38	23:47:04.68	29:28:44.01	73.1(4.8)	17.7(3.8)	34.6(5.6)	...	8.55	-1.57
39	23:46:59.63	29:28:42.48	93.1(3.9)	29.5(2.8)	80.2(1.7)	24.8(1.6)	26.4(3.5)	0.61	8.61	-1.53
40	23:47:07.88	29:28:41.83	1110(14)	...	1320(4)	419(3)	253(4)	0.71	8.62	-0.31
41	23:46:59.48	29:28:39.07	24.4(3.4)	9.62(2.79)	13.7(0.8)	4.86(1.10)	8.15(2.00)	0.22	8.64	-2.30
42	23:47:07.24	29:28:35.56	259(17)	...	83.6(3.2)	31.4(4.2)	70.7(5.6)	1.12	8.66	-1.51
43	23:47:02.31	29:28:35.50	795(73)	224(27)	1180(13)	407(8)	300(17)	1.65	8.64	-0.36
44	23:46:59.93	29:28:34.70	27.9(1.4)	10.7(1.2)	38.2(0.9)	13.7(0.8)	14.4(1.7)	0.21	8.66	-1.85
45	23:47:02.81	29:28:33.20	128(12)	33.7(5.9)	255(2)	97.4(1.8)	80.3(3.0)	0.62	8.66	-1.03
46	23:46:59.27	29:28:29.54	15.1(1.4)	5.00(1.23)	10.6(1.6)	...	8.63	-2.26
47	23:47:06.55	29:28:29.12	130(12)	11.5(5.0)	104(4)	33.9(2.9)	30.6(7.0)	1.01	8.62	-1.41
48	23:47:05.00	29:28:29.05	88.0(9.6)	7.38(7.25)	66.4(3.4)	26.0(3.0)	37.0(8.2)	0.98	8.67	-1.61
49	23:47:03.22	29:28:28.30	16.8(2.1)	6.18(4.07)	27.2(0.7)	14.3(0.7)	16.0(1.4)	0.03	8.74	-2.00
50	23:47:02.85	29:28:23.19	12.0(0.5)	4.05(0.65)	7.40(1.13)	...	8.63	-2.35
51	23:47:01.03	29:28:20.85	15.0(6.4)	8.40(9.18)	6.99(1.40)	2.59(1.09)	11.6(2.1)	0.50	8.65	-2.59
52	23:46:59.05	29:28:18.43	7.63(1.17)	2.10(1.17)	9.65(2.38)	...	8.58	-2.55
53	23:46:59.81	29:28:17.49	7.23(1.26)	0.841(0.649)	6.76(1.83)	...	8.37	-2.57
54	23:47:00.66	29:28:14.39	35.1(6.7)	...	0.683(0.781)	0.693(0.714)	11.6(2.3)	...	8.90	-3.60
55	23:46:58.84	29:28:13.90	95.6(9.5)	35.4(1.8)	61.3(1.3)	15.9(1.1)	16.9(2.1)	0.38	8.57	-1.65
56	23:46:59.58	29:28:07.99	63.0(7.9)	10.3(2.4)	10.5(1.5)	0.829(1.130)	21.6(2.5)	0.64	8.27	-2.41
57	23:46:58.90	29:27:59.14	5.50(3.03)	6.38(5.14)	7.15(1.30)	2.15(1.03)	11.3(1.7)	0.29	8.60	-2.58
58	23:46:59.41	29:27:57.92	13.5(1.3)	5.56(1.38)	13.5(2.3)	...	8.68	-2.30
59	23:46:59.62	29:27:53.87	3.44(0.87)	7.69(2.12)	23.9(1.9)	...	9.10	-2.90
60	23:46:59.17	29:27:52.85	3.99(1.65)	1.60(1.32)	11.8(1.7)	...	8.67	-2.83
61	23:46:58.64	29:27:50.82	13.0(2.5)	11.2(2.1)	30.8(1.6)	9.33(1.73)	15.3(1.9)	0.52	8.60	-1.94
62	23:47:00.19	29:27:47.75	3.24(0.71)	2.37(1.25)	18.4(1.8)	...	8.82	-2.92
63	23:46:58.04	29:27:37.83	1384(28)	420(7)	1110(7)	331(6)	252(8)	1.15	8.60	-0.39
64	23:46:58.63	29:27:35.26	1302(9)	300(4)	1380(4)	439(3)	291(6)	0.63	8.62	-0.29
65	23:46:58.11	29:27:34.74	2841(70)	527(24)	1730(11)	595(8)	526(15)	1.33	8.64	-0.19
66	23:46:58.91	29:27:31.93	1648(29)	307(13)	1240(8)	404(6)	339(12)	1.25	8.62	-0.34
67	23:46:58.32	29:27:31.74	2216(33)	285(16)	1190(9)	398(5)	324(9)	1.19	8.63	-0.36
68	23:46:58.54	29:27:31.73	344(9)	116(5)	650(2)	283(2)	297(5)	0.51	8.69	-0.62
69	23:46:58.88	29:27:28.81	1523(36)	274(17)	1060(9)	360(7)	355(12)	1.19	8.63	-0.41
70	23:47:07.56	29:26:54.13	60.9(7.3)	17.6(7.0)	33.8(1.4)	14.2(1.8)	34.7(4.2)	0.52	8.69	-1.90

Notes: Line fluxes are in the unit of $10^{-16} \text{ erg s}^{-1} \text{ cm}^{-2}$, after correcting for reddening and extinction. The values in brackets are the flux errors of the emission lines.

The newly designed MOS is based upon a mask plate with pinholes, which correspond to the targets. The mask replaces the slit plate in the spectroscopic system of BFOSC. The positions of pinholes are designed according to the astronomical coordinates of the targets and focus parameters of the telescope, and drilled with a precise drilling machine. The aperture of targets can be selected

with a diameter of $2.2''$, $2.7''$, $3.3''$ or $5.3''$ according to the seeing. To avoid blending in spectra, the separation of targets in terms of declination should be larger than $5.0''$. Within the FoV, 20–50 apertures can typically be drilled in a single mask, with a maximum of one hundred apertures in ideal cases. The grisms of MOS are the same as those of BFOSC.

The observing procedures for MOS are as follows. Beside the bias, flats and lamp spectra, the flat lamps are imaged without the grism in place to illuminate the masks and provide the identification of targets. A direct image of the target field is also obtained to be used as a comparison. For the observations of standard stars, an extra mask is designed with a series of apertures with different diameters and locations, which can cover the whole wavelength range of the targets in any mask. One standard star may be observed a total of three times with different locations, corresponding to the wavelength range from blue to red.

Our observations were carried out on the nights of 2012 September 15–17, using four multi-object masks with apertures of $2.7''$ in diameter. Two 1800 s exposures were acquired for each field using the G6 and G8 grisms, providing spectra covering the wavelength ranges of $\sim 3000\text{--}5100\text{ \AA}$ and $\sim 6000\text{--}8100\text{ \AA}$, respectively (the coverage depends on the spatial distribution of the targets). One 1800 s exposure offset from the galaxy was made for sky background. The seeing during the observations was $\sim 1.5''$. The G6 grism allowed us to cover the region around the [O II] $\lambda 3727$, H β , [O III] $\lambda 4959$ and [O III] $\lambda 5007$ lines with a spectral resolution of 8.0 \AA (full width at half maximum), and the G8 grism covers H α , [N II] $\lambda 6583$ and [S II] $\lambda\lambda 6717, 6731$ lines with a spectral resolution of 6.0 \AA .

2.3 Data Reduction And Emission Line Fluxes

The raw data were reduced with standard IRAF¹ routines and some customized IRAF scripts. The reduction of spectra included bias subtraction, flat-field correction, cosmic ray removal, spectral extraction, and wavelength and flux calibration. Different from normal long-slit spectra, wavelength ranges of multi-object masks changed with the spatial distribution of targets. We outline the key procedures here.

First, the spectra from one mask were extracted after the raw two-dimensional images were bias-subtracted and trimmed. The spectral flats were used to define the trace for all apertures, and wavelength calibration was obtained using Iron Argon (FeAr) arc lamp exposures taken throughout each night. Then, the flat spectra in the same mask were normalized to their combined spectrum and were used to remove variations in response and illumination. For each night, at least three exposures of the standard star HZ 4 were used for flux calibration, and each exposure was located in a different position of one standard-star mask to make sure the wavelengths could cover all of the ranges of our targets.

The spectral intensities with observed wavelengths were corrected for the Milky Way extinction; the Fitzpatrick (1999) extinction curve and the extinction $A(V) = 0.273$ in the V band from Schlafly & Finkbeiner (2011) were used.

Figure 2 illustrates a sample of the resulting spectra extracted from one mask. The root mean square (rms) noise of the continuum in the final corrected spectra is $\sim 1.0 \times 10^{-17}\text{ erg s}^{-1}\text{ cm}^{-2}\text{ \AA}^{-1}$. The spectrophotometric accuracy allows us to detect emission lines as weak as $\sim 10^{-16}\text{ erg s}^{-1}\text{ cm}^{-2}$. Emission line fluxes were measured from the individual spectra by simultaneously fitting Gaussian profiles to the [O II] $\lambda 3727$, H β , [O III] $\lambda 5007$, as well as H α , [N II] $\lambda 6583$ and [S II] $\lambda\lambda 6717, 6731$ lines with the SPLIT program in IRAF. Most emission lines were detected with signal-to-noise (S/N) ratios > 5 . For several H II regions, some lines in the blue part of the spectral range were below the detection limit.

¹ IRAF is the Image Reduction and Analysis Facility written and supported by the IRAF programming group at the National Optical Astronomy Observatory (NOAO) in Tucson, Arizona which is operated by AURA, Inc. under cooperative agreement with the National Science Foundation.

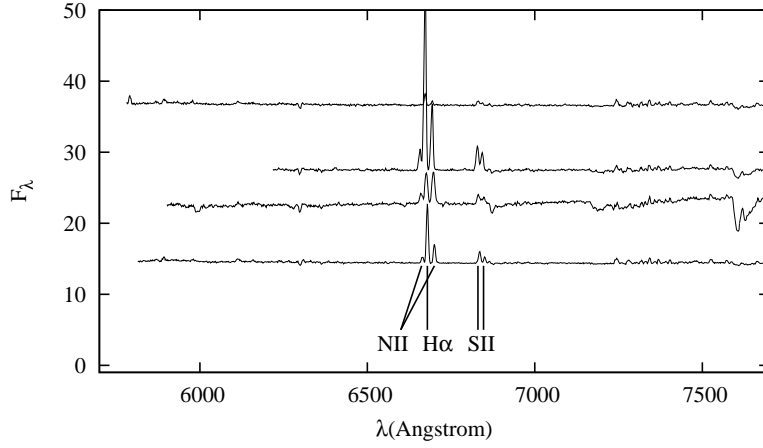


Fig. 2 Representative MOS spectra of H II regions in Arp 86. The spectra shown are from the same mask and observed with the G8 grism. In order to show the spectra in an orderly manner, they are arranged artificially in the plot and the fluxes are in units of $10^{-16} \text{ erg s}^{-1} \text{ cm}^{-2} \text{ Å}^{-1}$.

3 ANALYSES

3.1 Dust Extinction

The dust extinction was estimated in order to map the dust distribution in galaxies, to correct interstellar reddening for emission lines, and to achieve extinction-free SFRs using intrinsic $\text{H}\alpha$ luminosities. The $\text{H}\alpha/\text{H}\beta$ ratio was used to derive the value of interstellar reddening from the Balmer decrement, because the relative intensities of the Balmer lines are nearly independent of both density and temperature (Domínguez et al. 2013). The usual de-reddening procedure is to derive the logarithmic extinction at $\text{H}\beta$, $c(\beta)$, and it can be expressed by the following formula (Stasińska 2002)

$$c(\text{H}\beta) = \frac{R_{\text{H}\beta}}{R_{\text{H}\beta} - R_{\text{H}\alpha}} \log \left[\frac{(\text{H}\alpha/\text{H}\beta)_{\text{obs}}}{(\text{H}\alpha/\text{H}\beta)_{\text{int}}} \right], \quad (1)$$

where the subscript ‘obs’ and ‘int’ are the observed and corrected flux intensity ratios, respectively. We assumed the applicability of the Calzetti et al. (2000) extinction law, parameterized by $A_V = 4.0E(B - V)$ ($R_V \equiv A_V/E(B - V) = 4.0$, $R_{\text{H}\alpha} = 3.32$ and $R_{\text{H}\beta} = 4.60$). An intrinsic $\text{H}\alpha/\text{H}\beta$ ratio of 2.86 was assumed from the Case B recombination at 10^4 K (Osterbrock 1989).

Figure 3 shows the distribution of $c(\text{H}\beta)$ across the disks and bridge of the galaxy pair. We found that the nucleus of NGC 7753 has the highest dust extinction, and the extinction in the bulge region of this galaxy is also higher than in other regions. In most regions of NGC 7552, the extinction is $c(\text{H}\beta) \sim 1.0$, similar to that in the bulge of NGC 7753. However, the bridge has a much lower extinction of $c(\text{H}\beta) \sim 0.4$ than those of the disks, which may indicate the low dust and gas densities in this structure.

We corrected interstellar reddening for emission lines using the extinction obtained above. In a few cases ($\sim 1/5$ of the sample) where $\text{H}\beta$ was too faint to be measured reliably, the value from one or several nearby sources with a similar location was used. The extinction-corrected fluxes for the $[\text{O II}] \lambda 3727$, $[\text{O III}] \lambda 5007$, $\text{H}\alpha$, $[\text{N II}] \lambda 6583$ and $[\text{S II}] \lambda \lambda 6717, 6731$ emission lines are summarized in Table 1.

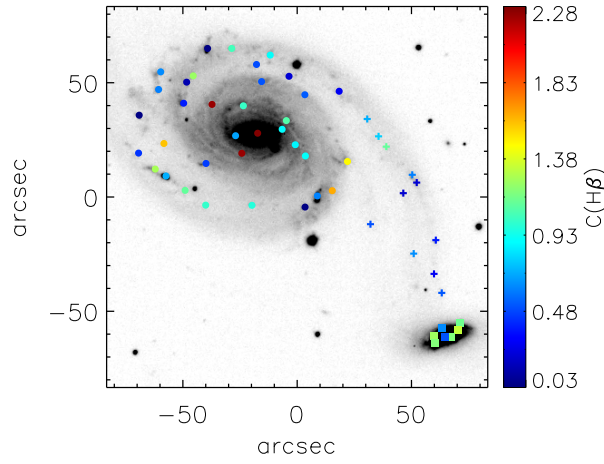


Fig. 3 The distribution of dust extinction $c(\text{H}\beta)$ across Arp 86. The symbols are the same as in Fig. 1, where circles are from NGC 7753, squares from NGC 7752 and pluses from the bridge.

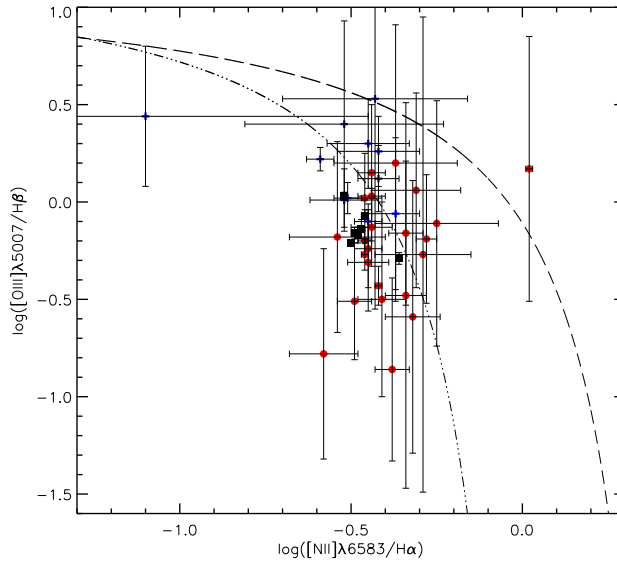


Fig. 4 Classical BPT diagram for H II regions with the demarcation between star-forming regions and active galactic nuclei (AGNs) from Kewley et al. (2001) (*long-dashed line*) and Kauffmann et al. (2003) (*dot-dot-dot-dashed line*). The symbols are the same as in Fig. 1.

3.2 Excitation Properties

We inspected the excitation properties of our sample of H II regions by plotting the $[\text{O III}] \lambda 5007/\text{H}\beta$ line ratio against the $[\text{N II}] \lambda 6583/\text{H}\alpha$ diagnostic diagram (BPT, Baldwin et al. 1981), as shown in Figure 4. The diagram includes two demarcation curves, i.e., the maximum starburst line from Kewley et al. (2001) and the pure star forming line from Kauffmann et al. (2003).

It can be seen that most of the regions are located under the maximum starburst line, and the sources in NGC 7752 are in the pure star forming region, indicating that star formation is the dominant ionizing source. The nucleus of NGC 7753 is the red point above the maximum starburst line, which shows AGN activity. Some regions from the bridge and NGC 7753 lying in the composite region may be ionized by star formation, but can also be linked to the presence of shocks, AGB stars and AGN photoionization.

3.3 Abundance Estimates

In order to quantify the distribution of metallicities in this interacting system, the abundance diagnostic $N2 = \log([N II] \lambda 6583/H\alpha)$ was adopted to derive oxygen abundances in H II regions. The N2 index has been studied by several groups (e.g., Storch-Bergmann et al. 1994; Raimann et al. 2000; Denicoló et al. 2002; Liang et al. 2006; Marino et al. 2013) and was confirmed to be a very useful indicator to calculate the oxygen abundance because of the close wavelength positions of these lines. We used the calibration from Pettini & Pagel (2004): $12 + \log(O/H) = 8.9 + 0.57 \times N2$.

The resulting oxygen abundance is presented in Figure 5. The center is located at the nucleus of NGC 7753, and the radius is normalized by the isophotal radius R_{25} of NGC 7753. As the figure shows, most sources share a similar O/H ratio from 8.5 to 8.8. The nucleus of NGC 7753 is higher than all the regions in its disk due to the presence of the AGN, which may act to bias the metallicity to a higher value due to its enhanced N2 index. The median metallicity of NGC 7752 is found to be ~ 8.63 , similar to most regions in NGC 7753. The H II regions in the bridge have very low flux densities and low S/N, thus they have large dispersion in the abundance mainly due to the large errors, and their average abundance is $12 + \log(O/H) \sim 8.65$.

Based on the abundances within the radius defined by R_{25} , we made a linear fit of the metallicity as a function of the radius to derive the radial gradient. The function is parameterized as $12 + \log(O/H) = a + b(R/R_{25})$. The resulting linear least-squares fit is represented by the red line in Figure 5, and can be expressed as $12 + \log(O/H) = 8.72(\pm 0.02) - 0.09(\pm 0.04)R/R_{25}$. The slope of the abundance gradient is $0.09 \text{ dex } R_{25}^{-1}$, approximately $-0.005 \text{ dex kpc}^{-1}$. This is a little steeper than the outside regions and NGC 7752, which are located above the red line.

3.4 Star Formation Activities

Active star formation is a striking feature in interacting systems. For Arp 86, we measured the SFR in each individual galaxy and H II region. The total SFRs were calculated using the mid-infrared luminosities from Smith et al. (2007) and the relation of Wu et al. (2005a) because the fluxes in the mid-infrared wavelength can be used as a proxy for star formation (Wu et al. 2005a; Zhu et al. 2008). The total SFRs are 8.6, 4.7 and $0.5 M_{\odot} \text{ yr}^{-1}$ for NGC 7753, NGC 7752 and the bridge region, respectively. The mean SFR surface densities (Σ_{SFR}) are 0.009, 0.081 and $0.003 M_{\odot} \text{ yr}^{-1} \text{ kpc}^{-1}$ for NGC 7753, NGC 7752 and the bridge region, respectively. The Σ_{SFR} in the companion galaxy is one order of magnitude higher than that in the main galaxy. The tidal bridge has the lowest SFR and Σ_{SFR} .

The SFRs for H II regions were calculated using the dust-corrected $H\alpha$ luminosity and the relation of Kennicutt (1998)

$$\text{SFR}_{H\alpha}(M_{\odot} \text{ yr}^{-1}) = 7.9 \times 10^{-42} [L(H\alpha)](\text{erg s}^{-1}), \quad (2)$$

which is calibrated using a Salpeter IMF with stellar masses in the range $0.1\text{--}100 M_{\odot}$, and stellar population models with solar abundances.

Figure 6 shows the detailed distribution of star formation activities in Arp 86. The left panel plots the SFRs with the background of the optical image. We found that the companion galaxy NGC 7752 is currently experiencing a galaxy-wide starburst with $\log(\text{SFR } M_{\odot} \text{ yr}^{-1}) = -0.6 \sim -0.3$ and

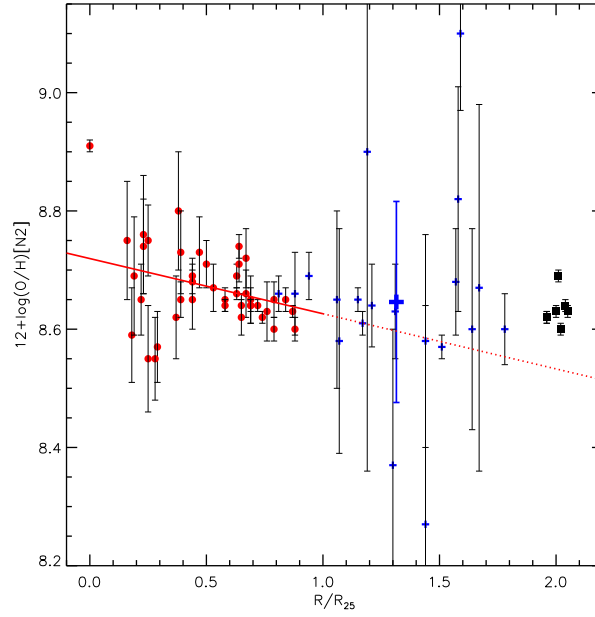


Fig. 5 Radial distribution of the oxygen abundance obtained from the N2 diagnostic. The red solid line is the linear least-squares fit of the H II regions in NGC 7753 (*red circles*), and the red dotted line is the extension of the former. The symbols are the same as in Figure 1. The mean abundance in the tidal bridge is marked with the large plus with a blue error bar.

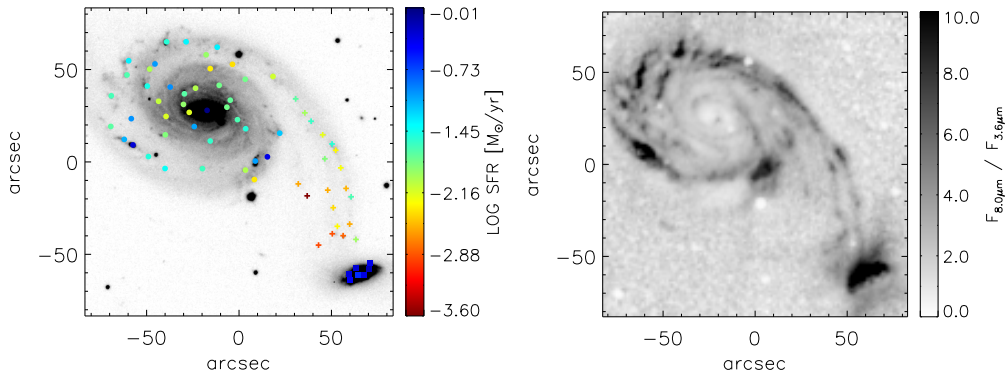


Fig. 6 Distribution of SFRs (*left*) and SSFRs (*right*) in Arp 86. In the left panel, the symbols are the same as in Figure 1 with the colors corresponding to the measured SFRs. In the right panel, SSFRs are indicated by the ratio of the 8.0 μm and 3.6 μm images of Arp 86.

$\Sigma_{\text{SFR}} = 0.5 - 1.2 M_{\odot} \text{ yr}^{-1} \text{ kpc}^{-1}$ for their H II regions. Most of the H II regions in NGC 7753 have $\log(\text{SFR } M_{\odot} \text{ yr}^{-1})$ lower than -1.0 except for the nucleus and two star-forming sources, which have similar SFRs to NGC 7752. However, the SFR in the nucleus of NGC 7753 may be overestimated due to the effect of the AGN. The star formation in the bridge is described by $\log(\text{SFR } M_{\odot} \text{ yr}^{-1}) \sim -2.5$ and has the lowest Σ_{SFR} in the interacting system, as expected.

In order to further explore the star formation activities in Arp 86, we presented the ratio map of its 8.0 μm and 3.6 μm images in the right panel of Figure 6. The two infrared images were taken from Smith et al. (2007) and observed by the *Spitzer Space Telescope* (Werner et al. 2004). Because the 3.6 μm luminosity provides an approximate measure of the stellar mass in the galaxy (Zhu et al. 2010) and the 8.0 μm luminosity can be used to trace star formation activities in galaxies, the ratio of the two images can be taken as the specific star formation rate (SSFR). From the ratio map, we found that the overall distribution of SSFRs in Arp 86 is similar to that of SFRs, where NGC 7752 has the highest SSFRs in the whole system and the two regions lying in the southern arm of NGC 7753 also obviously have high SSFRs. By contrast, the SSFR in the bulge region of NGC 7753 is very low, although there is a high SFR there.

3.5 Stellar Population

We used the spectral synthesis code STARLIGHT (Cid Fernandes et al. 2005; Mateus et al. 2006; Asari et al. 2007; Cid Fernandes et al. 2009) to derive the stellar populations of the target regions in Arp 86. This code fits an observed spectrum O_λ with a model M_λ which adds up a number of spectral components from a pre-defined set of base spectra. The base spectra consist of simple stellar populations (SSPs) from Bruzual & Charlot (2003), which have 25 ages from 0.001 to 18 Gyr and six metallicities from 0.005 to $2.5 Z_\odot$, summing up 150 SSPs.

The results of the spectral synthesis fitting are presented in Figure 7, where the distribution of stellar ages, weighted by the light fraction, is plotted. Because the spectra with low S/N may result in large errors, we divided the spectra into two classes based on S/N measured at 4730–4780 Å in Figure 7: $S/N \geq 3.0$ (in filled symbols) and $S/N < 3.0$ (in open symbols). We mainly consider the spectra with $S/N \geq 3.0$. It can be seen from Figure 7 that the ages of target regions in NGC 7752 are $\sim 10 - 100$ Myr, similar to the tidal bridge and some arm regions in NGC 7753. The ages of the bulge region in NGC 7753 are $\sim 1-10$ Gyr, according to the low SSFR mentioned in Section 3.4.

4 DISCUSSION

In the previous section we mainly illustrated the properties of abundances and star formation activities in the interacting galaxy pair Arp 86. The slope of the abundance gradient in the inner disk of NGC 7753 is less than $0.1 \text{ dex } R_{25}^{-1}$ along with a much shallower slope in the outer disk and tidal bridge. H II regions in NGC 7752 have higher SFRs than those in NGC 7753, by one order of magnitude. The stellar populations in NGC 7752 are in the age range $\sim 10 - 100$ Myr. These evidences indicate that more active star formation is ongoing in the companion galaxy than in the main galaxy. These results provide solid evidence that galaxy interactions play an important role in modifying the metallicity properties and star formation activities of galaxies.

Simulations indicate that tidal forces during encounters can cause large-scale gas inflows in galaxies (Barnes & Hernquist 1996), which can flatten the metallicity distributions (Rupke et al. 2010). Kewley et al. (2006) proposed a scenario in which galaxy interactions drive large gas inflows toward the central regions, where less enriched gas is carried from the outskirts of the galaxy into the central regions, disrupting metallicity gradients, and diluting central metallicities. Consistent with these models, our results from Figure 5 show a very flattened abundance gradient with a slope of $0.09 \pm 0.04 \text{ dex } R_{25}^{-1}$ in the inner disk of the main galaxy, which corresponds to $\sim 0.005 \text{ dex kpc}^{-1}$. The slope is one order of magnitude lower than the typical value of $0.03-0.10 \text{ dex kpc}^{-1}$ in normal spiral galaxies, such as NGC 628 (Gusev et al. 2014), NGC 3621 (Bresolin et al. 2012), M33 (Bresolin 2011) and M101 (Lin et al. 2013). Their observational results provide similar evidences. Kewley et al. (2010) systematically studied a sample of close galaxy pairs and found that the mean gradient in their galaxy pairs is $-0.25 \text{ dex } R_{25}^{-1}$ compared with a mean gradient of $0-0.67 \text{ dex } R_{25}^{-1}$ for the isolated spiral galaxies, and demonstrated that galaxy pairs have flatter metallicity gradients due to large tidal gas inflows in galaxy interactions and mergers.

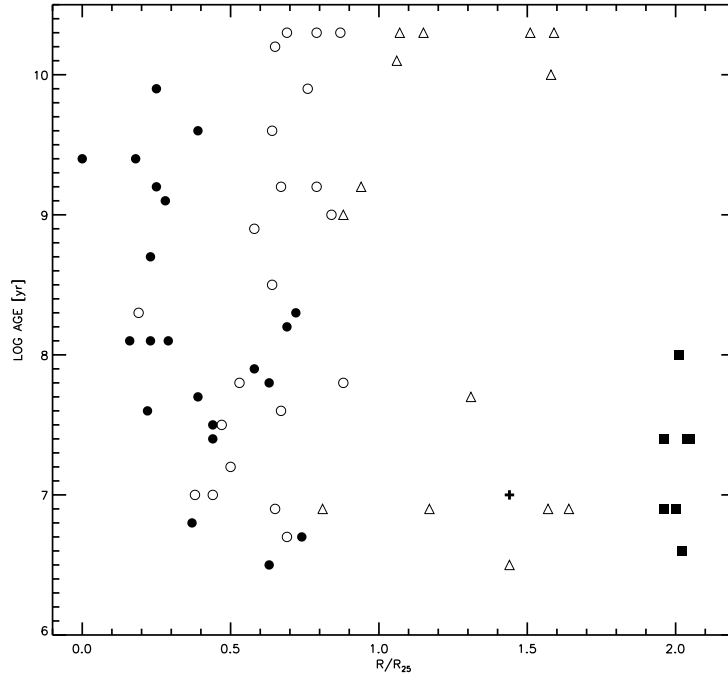


Fig. 7 Distribution of stellar ages in Arp 86. The ages are weighted by stellar luminosity (Cid Fernandes et al. 2005) and derived from spectral synthesis fitting. The filled symbols are the spectra with $S/N \geq 3.0$ (measured at 4730–4780 Å) and the open ones are the spectra with $S/N < 3.0$ (i.e., open circles are the regions in the galaxy NGC 7753, open triangles are the tidal bridge between the two galaxies).

Interaction-induced star formation has also been investigated by observations and models. In many sample and case studies, ultraviolet, H α and infrared images show enhanced star formation activities in interacting systems (e.g., Cao & Wu 2007; Smith et al. 2007). The simulations of Cox et al. (2008) found merger-driven star formation is a strong function of merger mass ratio, and the less massive companion is expected to be more susceptible to tidal forces and may have a larger enhancement of star formation.

In our results, Figures 6 and 7 show the same trend, where the SFRs of H II regions are one order of magnitude higher in NGC 7752 than in the main galaxy NGC 7753. Such evidences are also found in the NGC 7771+NGC 7770 interacting system (Alonso-Herrero et al. 2012) and statistics based on the Sloan Digital Sky Survey Data (Woods & Geller 2007).

Besides NGC 7753 and NGC 7752, the galaxy 2MASX J23470758+2926531 may be part of the Arp 86 system. This galaxy is visible in GALEX UV images (Smith et al. 2010), along with many optical images. Sengupta et al. (2009) estimated the stellar mass and H II mass of this galaxy, and found they are $2.9 \times 10^9 M_{\odot}$ and $4.5 \times 10^8 M_{\odot}$, respectively. The H I column density image shows a connection between NGC 7752 and 2MASX J23470758+2926531 (Sengupta et al. 2009). We also obtained the spectra of 2MASX J23470758+2926531, and found its redshift to be $z = 0.0166 \pm 0.0003$, which is similar to Arp 86 ($z \sim 0.0162$). It is located in the composite region of the BPT diagram, Σ_{SFR} is $\sim 0.027 M_{\odot} \text{ yr}^{-1} \text{ kpc}^{-1}$, and the oxygen abundance is similar to most of the regions in NGC 7753, which demonstrate that 2MASX J23470758+2926531 is a companion of NGC 7753.

5 SUMMARY

Optical MOS spectra of 69 H α regions located in the interacting system Arp 86 have been analyzed. The oxygen abundances, SFRs and stellar populations have been derived. We have found that the extinction in NGC 7552 and the bulge region of NGC 7753 is $c(H\beta) \sim 1.0$, higher than that in the bridge and outer disks of NGC 7753 ($c(H\beta) \sim 0.4 - 0.8$). The BPT diagram indicates that pure star formation activity is occurring in NGC 7752 and AGN activity is in the nucleus of NGC 7753.

The oxygen abundances estimated from the N2 metallicity indicator yield a similar O/H ratio from 8.5 to 8.8 in most H II regions. The slope of the abundance gradient in the inner disk of NGC 7753 is less than 0.1 dex R_{25}^{-1} along with a much shallower slope in the outer disk and tidal bridge, demonstrating that tidal forces during encounters can flatten the metallicity distributions.

The total SFRs are 8.6, 4.7 and 0.5 $M_{\odot} \text{ yr}^{-1}$ for NGC 7753, NGC 7752 and the bridge region, respectively. The companion galaxy NGC 7752 is currently experiencing a galaxy-wide starburst with $\log(\text{SFR } M_{\odot} \text{ yr}^{-1}) = -0.6 \sim -0.3$ and $\Sigma_{\text{SFR}} = 0.5 - 1.2 M_{\odot} \text{ yr}^{-1} \text{ kpc}^{-1}$ for their H II regions. We have also found that the Σ_{SFR} values of H II regions are one order of magnitude higher in NGC 7752 than in the main galaxy NGC 7753, and the stellar population of NGC 7752 is also as young as 10–100 Myr, predicting that the companion galaxy is more susceptible to the effects of the interaction than the primary.

We also have observed the spectra of the galaxy 2MASX J23470758+2926531, and have found that this galaxy has a similar redshift to Arp 86, and its abundance and star formation properties are similar to NGC 7753, indicating it may be a part of the Arp 86 system.

Acknowledgements We are grateful to the anonymous referee for their thoughtful comments and insightful suggestions that helped to improve this paper. We thank the kind staff at the Xinglong 2.16 m telescope for their support during the observations. This project is supported by the National Natural Science Foundation of China (Grant Nos. 11078017, 11303038 and 11433005), and by the Strategic Priority Research Program “The Emergence of Cosmological Structures” of the Chinese Academy of Sciences (Grant No. XDB09000000). We made extensive use of the NASA/IPAC Extragalactic Database (NED) which is operated by the Jet Propulsion Laboratory, California Institute of Technology, under contract with the National Aeronautics and Space Administration.

References

- Alonso-Herrero, A., Rosales-Ortega, F. F., Sánchez, S. F., et al. 2012, MNRAS, 425, L46
 Asari, N. V., Cid Fernandes, R., Stasińska, G., et al. 2007, MNRAS, 381, 263
 Baldwin, J. A., Phillips, M. M., & Terlevich, R. 1981, PASP, 93, 5
 Barnes, J. E., & Hernquist, L. 1992, ARA&A, 30, 705
 Barnes, J. E., & Hernquist, L. 1996, ApJ, 471, 115
 Bresolin, F. 2011, ApJ, 730, 129
 Bresolin, F., Kennicutt, R. C., & Ryan-Weber, E. 2012, ApJ, 750, 122
 Bruzual, G., & Charlot, S. 2003, MNRAS, 344, 1000
 Calzetti, D., Armus, L., Bohlin, R. C., et al. 2000, ApJ, 533, 682
 Cao, C., & Wu, H. 2007, AJ, 133, 1710
 Cid Fernandes, R., Mateus, A., Sodré, L., Stasińska, G., & Gomes, J. M. 2005, MNRAS, 358, 363
 Cid Fernandes, R., Schoenell, W., Gomes, J. M., et al. 2009, in Revista Mexicana de Astronomía y Astrofísica Conference Series, 35, 127
 Denicoló, G., Terlevich, R., & Terlevich, E. 2002, MNRAS, 330, 69
 Domínguez, A., Siana, B., Henry, A. L., et al. 2013, ApJ, 763, 145
 Fitzpatrick, E. L. 1999, PASP, 111, 63
 Gusev, A. S., Egorov, O. V., & Sakhibov, F. 2014, MNRAS, 437, 1337

- Hopkins, P. F., Bundy, K., Croton, D., et al. 2010, *ApJ*, 715, 202
- Kauffmann, G., Heckman, T. M., Tremonti, C., et al. 2003, *MNRAS*, 346, 1055
- Kennicutt, R. C., Jr. 1998, *ARA&A*, 36, 189
- Kewley, L. J., Dopita, M. A., Sutherland, R. S., Heisler, C. A., & Trevena, J. 2001, *ApJ*, 556, 121
- Kewley, L. J., Geller, M. J., & Barton, E. J. 2006, *AJ*, 131, 2004
- Kewley, L. J., Rupke, D., Zahid, H. J., Geller, M. J., & Barton, E. J. 2010, *ApJ*, 721, L48
- Laurikainen, E., Salo, H., & Aparicio, A. 1993, *ApJ*, 410, 574
- Li, Y., Bresolin, F., & Kennicutt, R. C., Jr. 2013, *ApJ*, 766, 17
- Liang, Y. C., Yin, S. Y., Hammer, F., et al. 2006, *ApJ*, 652, 257
- Lin, L., Zou, H., Kong, X., et al. 2013, *ApJ*, 769, 127
- Marino, R. A., Rosales-Ortega, F. F., Sánchez, S. F., et al. 2013, *A&A*, 559, A114
- Mateus, A., Sodr , L., Cid Fernandes, R., et al. 2006, *MNRAS*, 370, 721
- Osterbrock, D. E. 1989, *Astrophysics of Gaseous Nebulae and Active Galactic Nuclei* (Mill Valley, CA: University Science Books)
- Osterbrock, D. E., & Ferland, G. J. 2006, *Astrophysics of Gaseous Nebulae and Active Galactic Nuclei*, eds. Osterbrock, D. E., & Ferland, G. J. (Sausalito, CA: University Science Books)
- Pettini, M., & Pagel, B. E. J. 2004, *MNRAS*, 348, L59
- Raimann, D., Storch-Bergmann, T., Bica, E., Melnick, J., & Schmitt, H. 2000, *MNRAS*, 316, 559
- Rupke, D. S. N., Kewley, L. J., & Barnes, J. E. 2010, *ApJ*, 710, L156
- Sanders, D. B., Mazzarella, J. M., Kim, D.-C., Surace, J. A., & Soifer, B. T. 2003, *AJ*, 126, 1607
- Schlafly, E. F., & Finkbeiner, D. P. 2011, *ApJ*, 737, 103
- Sengupta, C., Dwarakanath, K. S., & Saikia, D. J. 2009, *MNRAS*, 397, 548
- Smith, B. J., Struck, C., Hancock, M., et al. 2007, *AJ*, 133, 791
- Smith, B. J., Giroux, M. L., Struck, C., & Hancock, M. 2010, *AJ*, 139, 1212
- Stasi ska, G. 2002, Lectures to be published in the proceedings of the XIII Canary Islands Winter School of Astrophysics (arXiv:astro-ph/0207500)
- Storch-Bergmann, T., Calzetti, D., & Kinney, A. L. 1994, *ApJ*, 429, 572
- Struck, C., & Smith, B. J. 2003, *ApJ*, 589, 157
- Werner, M. W., Roellig, T. L., Low, F. J., et al. 2004, *ApJS*, 154, 1
- Woods, D. F., & Geller, M. J. 2007, *AJ*, 134, 527
- Wu, H., Cao, C., Hao, C.-N., et al. 2005a, *ApJ*, 632, L79
- Wu, H., Shao, Z., Mo, H. J., Xia, X., & Deng, Z. 2005b, *ApJ*, 622, 244
- Zhou, Z.-M., Cao, C., Meng, X.-M., & Wu, H. 2011, *AJ*, 142, 38
- Zhu, Y.-N., Wu, H., Cao, C., & Li, H.-N. 2008, *ApJ*, 686, 155
- Zhu, Y.-N., Wu, H., Li, H.-N., & Cao, C. 2010, *RAA (Research in Astronomy and Astrophysics)*, 10, 329